

Competition and selectivity during parallel evolution of bromine, chlorine and oxygen on IrO_x electrodes

Vos, Johannes G.; Venugopal, Anirudh; Smith, Wilson A.; Koper, Marc T.M.

DOI

[10.1016/j.jcat.2020.05.024](https://doi.org/10.1016/j.jcat.2020.05.024)

Publication date

2020

Document Version

Final published version

Published in

Journal of Catalysis

Citation (APA)

Vos, J. G., Venugopal, A., Smith, W. A., & Koper, M. T. M. (2020). Competition and selectivity during parallel evolution of bromine, chlorine and oxygen on IrO_x electrodes. *Journal of Catalysis*, 389, 99-110. <https://doi.org/10.1016/j.jcat.2020.05.024>

Important note

To cite this publication, please use the final published version (if applicable). Please check the document version above.

Copyright

Other than for strictly personal use, it is not permitted to download, forward or distribute the text or part of it, without the consent of the author(s) and/or copyright holder(s), unless the work is under an open content license such as Creative Commons.

Takedown policy

Please contact us and provide details if you believe this document breaches copyrights. We will remove access to the work immediately and investigate your claim.



Competition and selectivity during parallel evolution of bromine, chlorine and oxygen on IrO_x electrodes



Johannes G. Vos^a, Anirudh Venugopal^b, Wilson A. Smith^b, Marc T.M. Koper^{a,*}

^a Leiden Institute of Chemistry, Leiden University, PO Box 9502, 2300 RA Leiden, the Netherlands

^b Materials for Energy Conversion and Storage (MECS), Department of Chemical Engineering, Delft University of Technology, Van der Maasweg 9, 2629 HZ Delft, the Netherlands

ARTICLE INFO

Article history:

Received 21 March 2020

Revised 5 May 2020

Accepted 16 May 2020

Available online 26 May 2020

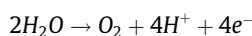
ABSTRACT

During hydrogen production for (renewable) energy storage, direct seawater electrolysis offers several notable advantages over freshwater electrolysis. Unfortunately, it is also hindered by possible oxidation reactions of chloride and (to a lesser extent) bromide, which can occur in parallel to the evolution of oxygen and form harmful by-products at the anode. Although the respective oxidation reactions of Br⁻ and Cl⁻ have been researched quite well on Pt, not much is known concerning bromide oxidation and its effect on the evolution of chlorine and oxygen for metal oxides, which are the class of electrocatalysts overwhelmingly used in industry. Using glassy carbon-supported iridium oxide (IrO_x) as a model system, we investigated the oxidation behaviour of this well-known oxygen evolution catalyst in an acidic Br⁻/Cl⁻ electrolyte. We first briefly discuss the solution chemistry and oxidation products that may be expected. Model studies were performed of the parallel evolution of Br₂, Cl₂ and O₂ to increase the understanding of the anodic competition problem, with a special focus on the selectivity towards oxygen. Using rotating ring-disk voltammetry and UV-Vis spectroscopy, our results suggest that bromide and chloride competitively absorb on IrO_x, but do not alter each other's oxidation reaction mechanisms, which both seem to adhere best to a Volmer-Heyrovský mechanism. We also find that bromide and chloride adsorption significantly slow down the oxygen evolution reaction, in an additive way. Even a relatively small amount of bromide highly affected the oxygen evolution selectivity. Formation of the interhalogen compound BrCl, which is possible in a mixed Br⁻/Cl⁻ electrolyte, does not seem to occur.

© 2020 The Authors. Published by Elsevier Inc. This is an open access article under the CC BY license (<http://creativecommons.org/licenses/by/4.0/>).

1. Introduction

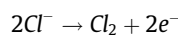
Water electrolysis is an attractive method for utilizing electricity from renewable energy sources, whose nature is highly intermittent [1–3]. In an acidic electrolyzer used for energy storage, H₂ is produced at the cathode; on the anode, the suitable reaction is the oxygen evolution reaction (OER), forming O₂ as an environmentally friendly byproduct according to



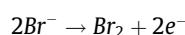
$$E_{\text{O}_2/\text{H}_2\text{O}}^0 = (1.229 - 0.059 \cdot \text{pH})\text{V} \text{ vs. NHE}$$

Large-scale electrolysis would require significant amounts of water as feedstock; at the same time, areas where the potential for renewable resources is the highest are usually at or near the sea, where freshwater is often a scarce commodity. Seawater, which is vastly more earth-abundant than freshwater, would thus be a much better substrate for use in large-scale electrolysis [4–6].

Unfortunately, the presence of chloride and, to a lesser extent, bromide, hampers the direct electrolysis of seawater, due to unwanted side-reactions [7–9]; both chloride and bromide can rapidly oxidize on the anode to form harmful byproducts. In acidic media, they react via the chlorine evolution reaction (CER) and bromine evolution reaction (BER):



$$E_{\text{Cl}_2/\text{Cl}^-}^0 = 1.358\text{V} \text{ vs. NHE}$$



$$E_{\text{Br}_2/\text{Br}^-}^0 = 1.087\text{V} \text{ vs. NHE}$$

Good OER catalysts tend to form chlorine as well, due to a scaling relationship between the CER and the OER [10–12]. This has been explained by the similar binding modes of oxygen and chlorine intermediates on OER catalysts. It is expected that a similar scaling exists between the BER and the OER. The BER and CER appear to have very similar reaction mechanisms on a variety of

* Corresponding author.

E-mail address: m.koper@chem.leidenuniv.nl (M.T.M. Koper).

surfaces [13–16], implying that their binding intermediates are similar in nature. The OER is a very sluggish reaction due to its complex four-electron nature, which means it has a significant overpotential. On the other hand, the CER and BER are two-electron reactions, with intrinsically faster kinetics compared to the OER; their overpotential can be vanishingly small [17].

The OER and its applicability to renewable energy conversion is currently receiving considerable scientific interest [18–20]. The CER has also been much studied for the chlor-alkali process, because chlorine is a key step towards the production of bleach and in bulk chemical manufacturing [21,22]. In the electrochemical formation of chlorine, the OER is a parasitic side-reaction that needs to be avoided. In contrast, the BER has received much less attention, although there has recently been some interest in its use in redox flow batteries [23,24]. The BER is also important during the treatment of wastewater, where its occurrence is strongly correlated with the formation of toxic brominated derivatives of organic components [25–27]. Its standard potential is quite low relative to the CER and OER, such that bromide oxidation can easily occur on an anode where the CER or OER are taking place.

Despite particular relevance to (sea)water electrolysis and water treatment, the simultaneous evolution of Br_2 , Cl_2 and O_2 has been little explored [28–30]. The BER is generally ignored in the context of seawater electrolysis, because the Br^- concentration in seawater has a relatively low value of 0.3%mol relative to the chloride concentration [31]. The occurrence of the BER alongside the CER is nonetheless a highly interesting phenomenon, which we have studied previously on Pt electrodes [32]. On a Pt electrocatalyst, we found that bromide adsorption leads to a profound change in the mechanism of chlorine evolution. We also observed the formation of the interhalogen compound BrCl , which likely results from a Langmuir-Hinshelwood-like recombination of adsorbed Br and Cl. Metal oxides are usually more popular catalysts than Pt regarding the industrial application of the OER; it would therefore be interesting to study the BER in aqueous chloride solutions on a metal oxide catalyst, especially since bromide oxidation on such materials has been the subject of only a few studies [16].

In this paper, we study the parallel evolution of Br_2 and Cl_2 during O_2 evolution in acidic media ($\text{pH} \approx 0.35$), where the BER and CER are in direct competition with the OER, and where they can be studied with minimum interference from reactions that lead to oxygenated halogen species, such as BrO_3^- or ClO^- [33–35]. We chose an amorphous, nano-particulate IrO_x catalyst as a model material, because virtually every known material that shows both OER activity and stability under acidic conditions is based on metal oxides containing Ir. Supported on GC, IrO_x has shown considerable activity for the CER and OER and some remarkable CER selectivity trends as a function of $[\text{Cl}^-]$ in the electrolyte. The latter has been studied previously by using a rotating ring-disk electrode (RRDE) technique where the Pt ring served as a detector for Cl_2 evolved [36]. Using a similar approach, we were interested in measuring the effect of Br^- and the BER on the OER and CER, where the rates of each reaction could be determined with the aid of the Pt ring, combined with modeling. The IrO_x electrocatalyst could also be conveniently electrodeposited as optically transparent thin layers. This allowed analysis of the identities of halogen oxidation products near stationary electrode surfaces using on-line transmission UV–Vis experiments.

2. Experimental

All experiments were carried out at room temperature ($\sim 20^\circ\text{C}$). RRDE experiments are inherently more susceptible to contamination than stationary UV–Vis experiments. Cleaning preparations

for forced convection experiments were thus significantly more laborative.

2.1. Chemicals

For the RRDE experiments, HClO_4 (70%, Suprapur[®]/Trace analysis grade) KHSO_4 (EMSURE/Analysis grade), KCl (EMSURE/Analysis grade) and HCl (30%, Ultrapur[®]/Trace analysis grade) were purchased from Merck. HBr (47%, Normapur[®]/Analysis grade) was purchased from VWR Chemicals. For the UV–Vis experiments, HClO_4 (60%, EMSURE/Analysis grade), HCl (32%, EMSURE/Analysis grade) and HBr (47%, EMSURE/Analysis grade) were purchased from Merck. Na_2IrCl_6 (99.9%, trace metals basis) and NaOH (30% solution, TraceSelect) were purchased from Sigma-Aldrich. All purchased chemicals were used as received. The water used for all experiments was prepared by a Merck Millipore Milli-Q system (resistivity 18.2 M Ωcm , TOC < 5 p.p.b.).

2.2. Cleaning procedures

All glassware in the RRDE experiments was boiled in a 3:1 mixture of concentrated H_2SO_4 and HNO_3 before first-time use. When not in use, all glassware was stored in a 0.5 M H_2SO_4 solution containing 1 g/L KMnO_4 . Before each RRDE experiment, all glassware was first rinsed with water, and then submerged in a dilute (~ 0.01 M) solution of H_2SO_4 and H_2O_2 to remove all traces of KMnO_4 and MnO_2 . It was then rinsed three times with water and boiled in water. The final rinsing-boiling procedure was repeated two more times.

The glassware and custom-built PTFE cell for UV–Vis experiments were cleaned by soaking in warm reagent grade 98% H_2SO_4 for an hour, followed by thorough rinsing with Milli-Q water and boiling three times in Milli-Q water. When not in use, they were stored submerged in Milli-Q water.

2.3. Electrode preparation

2.3.1. RRDE experiments

IrO_x/GC electrodes were prepared via electroflocculation of IrO_x nanoparticles, using a meta-stable IrO_x colloid suspension obtained from alkaline hydrolysis of $\text{Na}_2\text{Ir}[\text{Cl}]_6$ [37–40]. To prepare the IrO_x colloid, a light yellow solution of 2 mM Na_2IrCl_6 in 0.1 M NaOH was heated in a water bath to 70°C under continuous stirring, and kept at this temperature for 20 min, during which the solution turned a very faint blue. It was subsequently transferred to an ice bath and 70% HClO_4 was added under stirring, until the solution pH was approximately 1.5. The now dark violet solution was stirred in the ice bath for 30 min, allowing condensation of hydrated IrO_x colloids. This solution could then be used immediately for experiments. For long term storage, the solution was made alkaline ($\text{pH} \approx 13$) by addition of 30% NaOH, causing a subtle color shift from violet to purple. It could be stored for at least 3 months at 4°C .

To prepare the thin film IrO_x/GC electrode, the IrO_x particles were electroflocculated on the GC surface under rotation. An aliquot of the alkaline colloid solution was re-acidified with 70% HClO_4 down to $\text{pH} \approx 1.5$, leading again to a solution color change from purple to greyish violet. Care must be taken not to make the IrO_x solution too acidic, since competing CER at low pH may interfere with the reproducibility of the deposition. (CER originates from Cl^- in the solution, which is present as a byproduct from the Na_2IrCl_6 hydrolysis.) GC disks (Pine Research Instrumentation, surface area 0.196 cm^2) were prepared to a mirror finish by hand polishing with diamond pastes down to 0.05 μm particle size, followed by rinsing and sonication of the electrode in water for 3 min. IrO_x deposition was then performed in the acidic IrO_x colloid

solution at a rotation rate of 900 RPM, on a freshly prepared GC surface. A LowProfile Ag/AgCl electrode (Pine Research) was used as reference, the counter electrode was a Pt coil placed axisymmetrically under the RRDE tip. The disk electrode was first scanned at 250 mV s^{-1} in the potential range of 0.16–1.36 V vs. Ag/AgCl, to observe initial IrO_x deposition coupled to increasing OER and CER catalysis. Subsequently, amperometry was performed at 1.255 V vs. Ag/AgCl for 300 s, at a potential 10 mV positive of the approximate onset of mixed OER and CER. Currents rising over time indicated further IrO_x deposition. After deposition, a reflective blue film was visible on the GC surface.

Before each experiment, the IrO_x surface was subjected to a pre-treatment step to ensure reproducible activity (see Fig. S2 in the Supporting Information). The electrode was first kept at 0 V vs. RHE for 10 s, followed by a 3 s hold at 0.9 V, to equilibrate the electrode and allow pseudocapacitive charging to decay to a minimum. Scanning commenced immediately afterwards. The Pt ring electrode was electropolished before experiments by scanning from -0.1 V to 1.7 V at 500 mV s^{-1} for 20 scans at 1500 RPM, followed by removal of gas bubbles adhered to the tip [41]. Ring currents were corrected for constant background currents and product collection delay. The latter arises from the time needed for products formed on the disk to reach the ring, and was empirically determined for each investigated rotation rate.

2.3.2. UV-Vis experiments

Conductive fluorine doped tin oxide (FTO) substrates (TEC-15) were purchased from Hartford glass co. The FTO substrates were cleaned by sonication, using a sequence of laboratory soap, Milli-Q water, acetone, isopropanol and water, followed by drying the substrates with compressed air. IrO_x deposition was then performed using the same prepared colloid solutions and voltammetry-amperometry protocol described in Section 2.3.1. The FTO substrates were placed upright in the solution, with a LowProfile Ag/AgCl reference electrode aligned to the centre of the electroactive surface and a circular Pt counter electrode placed symmetrically around the bottom. Instead of a rotating tip, a stirrer bar at the bottom of the cell rotating at $\sim 400 \text{ RPM}$ was used to induce mass flow of the IrO_x particles during deposition.

2.4. Cell preparation

2.4.1. RRDE experiments

An IviumStat potentiostat (Ivium Technologies) with IviumSoft software was used in all experiments for potential control. The electrode assemblies were E6 ChangeDisk RRDE tips with a PEEK shroud, attached to a MSR rotator (Pine Research). All experiments were 95% iR-compensated in-situ, by measuring the solution resistance with electrochemical impedance spectroscopy at 0.90 V vs. RHE on the disk, and observing the absolute impedance in the high frequency domain (100–50 KHz) corresponding to a zero-degree phase angle. All used solutions were saturated and continuously bubbled with Ar gas (Linde, purity 6.0) during experiments. The reference electrode was a HydroFlex[®] reversible hydrogen electrode (Gaskatel), separated from the main solution using a Luggin capillary, with the capillary tip purposely aligned to the center of the working electrode [42]. An additional LowProfile Ag/AgCl reference electrode served to measure the solution pH and was used for interconversion between the NHE and RHE scale. The Ag/AgCl reference was externally calibrated on a regular basis and had a value of $199 \pm 0.5 \text{ mV}$ vs. NHE. A Pt mesh was used as counter electrode, separated from the main solution by a coarse sintered glass frit.

2.4.2. UV-Vis experiments

A Vertex potentiostat (Ivium Technologies) run by the IviumSoft software package was used for potential control. Transmission

measurements were performed in a custom-built setup, consisting of a PTFE electrochemical cell housing equipped with quartz windows. A coiled platinum wire was used as the counter electrode, and a LowProfile Ag/AgCl reference electrode (Pine Research) was placed in fixed position relative to the IrO_x /FTO working electrode. The Ag/AgCl electrode was calibrated at $199 \pm 1 \text{ mV}$ vs. NHE. All applied potentials were 90% iR-compensated according to the solution resistance, which was measured using a similar procedure as in Section 2.4.1. To achieve a wide spectrum in the incoming beam, a deuterium lamp (Mikropack D-2000) and a halogen lamp (Ocean Optics HL 2000 – FHSA), were used in the setup. These light sources were combined using an optical fiber arrangement and this fiber acted as the illumination source for the transmission measurements. A Maya 2000 Pro spectrometer (Ocean Optics) was used to capture the transmitted light. The setup was aligned in such a way that the IrO_x /FTO samples were illuminated from the back side and the transmitted light was captured on the opposite side of the electrochemical cell. The transmission data was recorded simultaneously with the electrochemical measurements. High rates of oxygen evolution at high potentials occasionally posed a problem, because the poor solubility of oxygen led to O_2 bubbles forming on the window, deflecting the beam. Within the potential limits of the reported results, O_2 bubble formation did not occur.

3. Results and discussion

3.1. Parallel RRDE oxidation currents as function of chloride concentration

We will first describe our methods and a few general results regarding the parallel oxidation of Br^- , Cl^- and H_2O on the IrO_x /GC catalyst. RRDE cyclic voltammetry was used for all kinetic studies, since both the BER and CER are rapid reactions which quickly become diffusion controlled as the overpotential increases. Hydrodynamic conditions keep the diffusion layer thickness constant in time, simplifying the analysis and allowing a deeper investigation into the role of mass transport. Sufficiently high rotation rates also prevented follow-up reactions related to Br^- by removing Br_2 formed near the surface (see below). With the RRDE, it was possible to use a Pt ring to selectively reduce halogen species formed in parallel with OER, so that the reactions can be separated and analyzed independently. The ring potential was fixed at 0.70 V vs. RHE, where the reduction of oxygen is negligible in presence of Br^- [43]. We previously found that the reduction of Br_2 and Cl_2 on Pt become diffusion limited at overpotentials of $\eta \approx 150 \text{ mV}$ and $\eta \approx 250 \text{ mV}$, respectively [32]. Halogen reduction reactions should thus be fully diffusion limited at 0.70 V vs. RHE, so that ring currents are quantitative.

All experimental data were gathered using cyclic voltammograms recorded at 10 mV s^{-1} . Forward scans were used for catalytic analysis, while forward and backward scans were used to estimate capacitive currents. These non-catalytic contributions were usually a minor factor (<0.1%) in the total current; they were minimized by subtracting a constant value from the forward scan currents. Results were recorded versus the RHE, which this is the 'natural' potential scale of the pH-dependent OER; we will generally use this scale to report OER-related results. The studied halogen evolution reactions are however pH-independent; a relatively acidic supporting electrolyte of 0.5 M HClO_4 ($\text{pH} \approx 0.35$) was used to reduce pH changes from the addition of HBr or HCl . Data involving Br^- or Cl^- oxidation are reported versus the NHE scale to account for potential shifts from pH effects, which were very minor (<5 mV). To exclude possible effects from variation in the electrochemically active surface area [44], data of each figure were measured on identical IrO_x films.

Fig. 1A shows some typical results measured on GC-supported IrO_x in a mixed Br^- and Cl^- electrolyte. The onset of bromide oxidation from 10 mM HBr is clearly visible around 1.12 V vs. RHE,

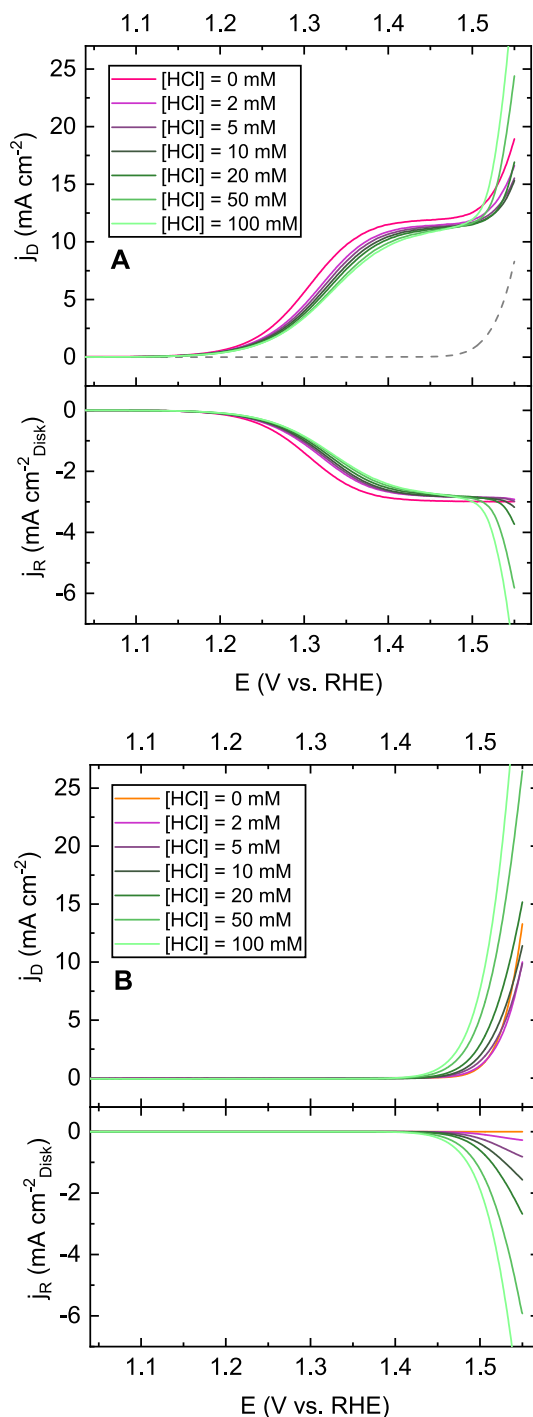


Fig. 1. Measured current densities of OER and halogen evolution on an IrO_x/GC electrode in 0.5 M HClO_4 . Top panels show forward, pseudo-capacitance corrected scans of the disk, lower panels show corresponding ring signals measured at 0.70 V vs RHE, corrected for background and collection delay. The effect of increasing HCl concentration is shown from black to green. A: OER in parallel with Br^- and Cl^- oxidation, in presence of 10 mM HBr and 0 – 100 mM HCl. Results in chloride-free conditions (only the BER and OER) are shown in pink. Also shown is the OER activity in absence of both Br^- and Cl^- (grey dotted trace). B: Experiments similar to A, but in Br^- -free conditions, with the ring at 0.95 V vs. RHE. Orange trace shows OER activity in absence of Cl^- . Solution purged with Ar, rotation rate 1600 RPM, CV's recorded at 50 mV s^{-1} .

and the reaction reaches a plateau near 1.40 V vs. RHE. This plateau stems from diffusion limitations, because its current density is about 95% of the limiting value predicted by the Levich equation. The OER starts around 1.45 V vs. RHE in absence of HBr and HCl (dotted trace in upper panel). In presence of 10 mM HBr (pink trace in upper panel), the OER appears superimposed on the limiting current of bromide oxidation; a closer inspection shows that its onset is at a slightly higher potential, and the activity is lower than in absence of Br^- . As intended, the OER is not captured in the corresponding ring data (lower panel), which only detects the limiting current of bromine evolution.

When HCl is also added, the ring data in Fig. 1A show an additional halogen oxidation reaction around 1.45 V vs. RHE, which suggests chloride oxidation starts taking place in parallel with OER. The CER activity is significantly lower than in Fig. 1B (which shows the parallel evolution of O_2 and Cl_2 in absence of bromide under otherwise identical conditions), and has a much higher onset potential. Reciprocally, HCl also imparts some notable changes on the bromide oxidation wave. The bromide oxidation activity is lowered in the whole measured potential range, which becomes more obvious with increasing $[\text{Cl}^-]$. As the results in Fig. 1 were all measured on an identical IrO_x film, they should be free from surface area variation effects. Diffusion limitations for bromide oxidation are again apparent around 1.40 V vs. RHE. Although bromide and chloride are now being oxidized simultaneously, there is no immediate sign of a new onset somewhere in-between the BER and CER, as we observed on Pt in previous work [32]. This suggests that no interhalogen reactions are taking place.

3.2. Brief review of microkinetic models

To gain deeper insight into the interplay between the halogen oxidation reactions and the OER, we primarily consider Tafel slopes (b) and reaction orders (\mathcal{R}). These quantities, defined as $b = \frac{\partial \eta}{\partial \log(j)}$ and $\mathcal{R} = \frac{\partial \ln(j)}{\partial \ln([\text{Cl}^-])}$, are easily accessible through experiment and thus convenient diagnostic tools for the underlying kinetics. To illustrate this, we will briefly consider previously described models for two-step electrochemical reactions, which will be discussed in the specific context of the CER, but are also relevant to other two-step mechanisms such as the BER or the hydrogen evolution reaction.

The mechanism of the CER on metal oxides is usually thought to adhere to two types of rate-limiting steps, originally proposed by Heyrovský and Krishtalik [45]. It is assumed that the rate-limiting step is preceded by the adsorption and discharge of a chloride ion, which can be termed the Volmer step:



Here, $*$ represents a free catalytic site, and Cl^* is a reactive chlorine intermediate adsorbed on the surface. The exact nature of $*$ and Cl^* in Eq. (1) has not been completely resolved; they are probably intricately coupled to the surface chemistry of the oxide as the rate of reaction 1 has been shown to be slowed down by H^+ in very high concentrations [46,47]. Eq. (1) is thus likely a simplification, but the steps it represents are not rate-limiting as long as extremely low pH (<0) is avoided. The Cl^* coverage θ_{Cl} is then in quasi-equilibrium and can be written as a fraction (between 0 and 1) of the 'maximum coverage'. In the mean-field Langmuir approximation it is given by: [48]

$$\theta_{\text{Cl}} = \frac{K_{\text{Cl}}[\text{Cl}^-]e^{\eta}}{K_{\text{Cl}}[\text{Cl}^-]e^{\eta} + 1} \quad (2)$$

In Eq. (2), η is an overpotential defined as $\eta = E - E^0$, where E is the applied potential, and E^0 is any convenient reference potential,

such as the standard potential of the overall reaction. K_{Cl} is then the chloride adsorption constant at $\eta = 0$, and $f = F/(RT)$.

In the Heyrovský step, the evolution of a Cl_2 molecule results from an electron transfer reaction between Cl^* and a second Cl^- ion from solution, reminiscent of the Eley–Rideal mechanism in heterogeneous gas-phase reactions:



At overpotentials high enough that the backward reaction is negligible, the j vs. E relationship predicted by Eq. (3) can be written as

$$j_{VH} = Fk_H\theta_{Cl}e^{\alpha_H f\eta}[Cl^-] = Fk_H \frac{K_{Cl}[Cl^-]^2 e^{(\alpha_H+1)f\eta}}{K_{Cl}[Cl^-]e^{f\eta} + 1} \quad (4)$$

In the above, k_H is the rate constant of the Heyrovský reaction for $\eta = 0$, and α_H is the corresponding transfer coefficient. Alternatively, the Krishtalik mechanism assumes that desorption is a two-step process, involving a second type of chlorine intermediate:



The electron transfer in Eq. (5) is assumed to be rate-limiting relative to the (non-electrochemical) desorption step in Eq. (6), where the rather exotic chloronium (Cl^{*+}) intermediate is supposedly stabilized by the metal oxide surface, as its structure is usually proposed to be $(O - Cl^*)^+$. When again assuming that η is positive enough that the forward reaction dominates, Eq. (5) predicts that

$$j_{VK} = Fk_K\theta_{Cl}e^{\alpha_K f\eta} = Fk_K \frac{K_{Cl}[Cl^-]e^{(\alpha_K+1)f\eta}}{K_{Cl}[Cl^-]e^{f\eta} + 1} \quad (7)$$

where the symbols have similar meanings as in Eq. (4). Eq. (7) has a similar j vs. E relationship as Eq. (4), but it differs in its $[Cl^-]$ dependence. Finally, a third type of rate-limiting step has also often been described, termed the Tafel step:



This mechanism assumes that the reaction is fully dependent on surface-bound species, and that the rate-limiting step is non-electrochemical. It implies that the forward current density follows

$$j_{VT} = 2Fk_T(\theta_{Cl})^2 = 2Fk_T \left(\frac{K_{Cl}[Cl^-]e^{f\eta}}{K_{Cl}[Cl^-]e^{f\eta} + 1} \right)^2 \quad (9)$$

where k_T is the non-electrochemical rate constant for Cl^* recombination. The Volmer–Tafel mechanism is dominant during the CER on Pt, but is usually not considered on metal oxides. It has been included for completeness. Detailed predictions of b and the chloride reaction order \mathcal{R}_{Cl^-} for each mechanism are described in the SI.

Even though the mechanism of the CER on metal oxides has been studied extensively, some uncertainty remains. The main issue is that combined \mathcal{R}_{Cl^-} values and Tafel slopes often do not satisfactorily agree with predictions of either the Volmer–Heyrovský (V-H) or Volmer–Krishtalik (V-K) mechanisms. As can be seen from Eq. (2), the driving force for Cl^- adsorption depends on both the potential E and the bulk chloride concentration. As θ_{Cl} changes from 0 to 1 under the effect of increasing η and/or $[Cl^-]$, the V-H mechanism predicts that the chloride reaction order \mathcal{R}_{Cl^-} decreases from 2 to 1, and that the Tafel slope increases from ~ 40 mV/dec to ~ 120 mV/dec (under the assumption that $\alpha_H \approx 0.5$). Tafel slopes of ~ 40 mV/dec at low overpotentials have indeed often been observed in experiments, pointing to the theoretical limit of $\theta_{Cl} \approx 0$; however, the corresponding experimental values for \mathcal{R}_{Cl^-} were almost universally close to 1, suggesting the limit of $\theta_{Cl} \approx 1$ [10,45,47–51]. Often, they were also practically invariant versus

E and $[Cl^-]$. The V-K mechanism was in fact specifically invoked to account for this problem, as it predicts that $0 \leq \mathcal{R}_{Cl^-} \leq 1$, which is slightly more in-line with these results. Conway and Tilak have postulated that the CER mechanism on metal oxides follows rather the Volmer–Tafel mechanism [48], but this view is not widely shared. We will discuss our results in adherence with previous literature, although the established discrepancies between the models and experimental results must be kept in mind. We also remark that the Langmuir isotherm in Eq. (2) is likely an oversimplification, but that the use of a more complex isotherm, such as devised by Frumkin, does not change the previously described limits for b and \mathcal{R} when either $\theta \rightarrow 0$ or $\theta \rightarrow 1$. Their shape and width as function of E and $[Cl^-]$ will however depend sensitively on the isotherm. When discussing experimental findings, we will restrict ourselves mostly to some general trends and possible limiting values.

3.3. Kinetic analysis and reaction orders of bromide oxidation

We first investigate in more detail the bromide oxidation waves in Fig. 1 between 1.10 and 1.45 V vs. RHE. For this, Koutecký–Levich plots were constructed by varying the rotation rate (see Fig. S5 and Fig. S6) for each combination of $[HCl] + 10$ mM HBr. In these plots, the extent to which the y-intercepts approach zero can be unambiguously interpreted as a degree of mass transport control over the reaction, especially if the plots are highly linear.

Data in Fig. 2 were derived from measured disk current densities j_D , where up to 1.45 V, no evolution of Cl_2 or O_2 occurs. In the presence of Cl^- , formation of the interhalogen $BrCl$ is thermodynamically allowed around potentials >1.19 V vs. NHE [32]; we will discuss this issue further below, and for the moment refer to positive currents within 1.10–1.40 V vs. NHE in presence of Cl^- as ‘bromide oxidation’.

Fig. 2A shows that the BER (pink trace) is essentially fully diffusion controlled near 1.35 V vs. NHE (~ 1.38 V vs. RHE). When HCl is present, the intercept values become slightly larger as $[Cl^-]$ increases, indicating that the reaction becomes slightly more kinetically controlled and diffusion limitations are approached more slowly as a function of potential; the reaction nonetheless always becomes diffusion controlled above 1.40 V vs. NHE. In Fig. 2B, the BER (pink trace) shows a quasi-linear Tafel region between 1.15 and 1.25 V vs. NHE, where values are initially 90 mV/dec and gradually increase with potential. In this region, the effect of HCl is a slight increase of the Tafel slope values. All slopes increase sharply at potentials higher than 1.25 V vs. NHE, which can clearly be ascribed to the onset of mass transport control; the effect of Cl^- is a somewhat more extended potential window of kinetic control.

Fig. 3A shows chloride reaction orders (\mathcal{R}_{Cl^-}) for bromide oxidation at a constant $[HBr] = 10$ mM, derived from log-log plots of current density at constant potential (Fig. S12). Values for \mathcal{R}_{Cl^-} are always slightly negative, as also visualized by a reduction in bromide oxidation currents by Cl^- in the curves in Fig. 1A. Observing the quasi-linear Tafel slopes in Fig. 2B, the reaction is irreversible and kinetically controlled within 1.18–1.25 V vs. NHE; here, $\mathcal{R}_{Cl^-} \approx -0.1$, regardless of potential or chloride concentration. At higher potentials where diffusion limitations dominate, \mathcal{R}_{Cl^-} approaches 0. Fig. 3B furthermore shows bromide reaction orders (\mathcal{R}_{Br^-}) for the BER, in absence of Cl^- (see also Fig. S9). The BER, due to its rather high intrinsic rate, approaches diffusion limitations very quickly; this leads to only a narrow potential window of around 1.19–1.22 V in which the reaction was kinetically controlled at all measured bromide concentrations. Values of \mathcal{R}_{Br^-} within this window were found to be significantly higher than 1 at low concentrations, and leveled off to lower values as $[Br^-]$ increased. For diffusion-controlled potentials, $\mathcal{R}_{Br^-} \approx 1$, as can be expected when transport of Br^- to the surface is rate-limiting.

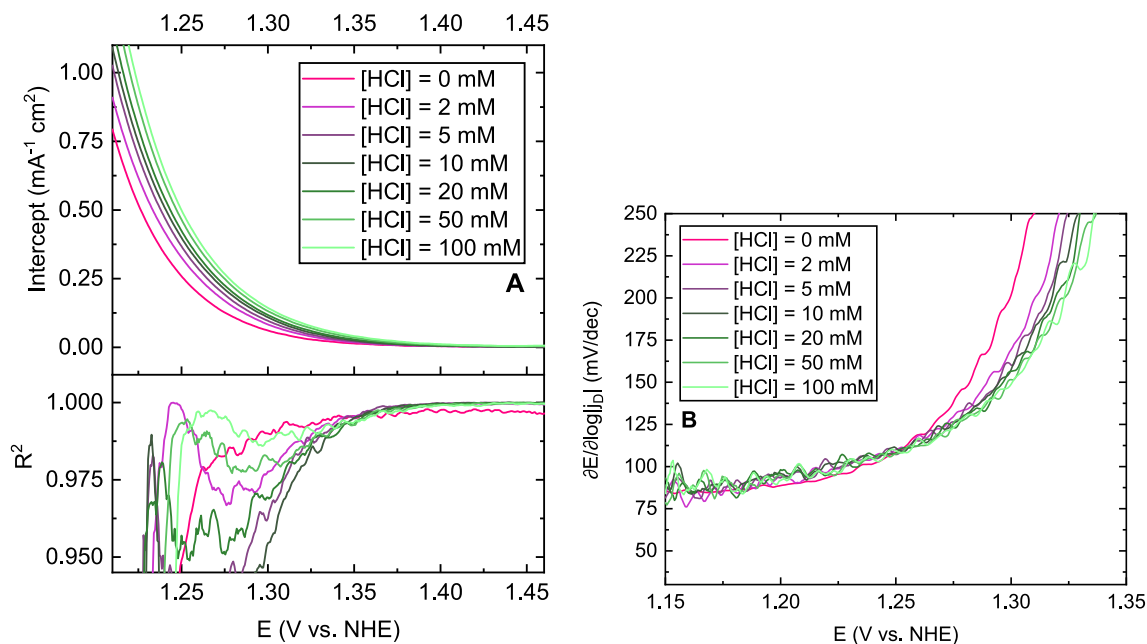


Fig. 2. Kinetic data measured in the potential region of bromide oxidation, in 0.5 M $HClO_4$ + 10 mM HBr, for varying concentrations of HCl. Data are shown on the NHE potential scale to account for minor (± 4 mV) pH shifts. A: Values of the intercept as function of potential, derived from Koutecký-Levich plots as in Fig. S6. Pink trace shows data when $[HCl] = 0$ mM. Top panel shows values of the intercept; lower panel shows corresponding values of the linear correlation coefficient R^2 . B: Tafel slopes obtained from semi-logarithmic data of Fig. 1 (see Fig. S11).

The \mathcal{R}_{Br^-} values in Fig. 3B are best captured by the V-H mechanism, as they are appreciably higher than 1, and (at kinetically controlled potentials) appear to level off to 1 as both E and $[Br^-]$ increase. However, within the Langmuir V-H or V-K formalism, the ‘onset value’ of ~ 90 mV/dec for Tafel slopes in Fig. 2B is quite different from the expected value of ~ 40 mV/dec at low overpotentials, provided that $\alpha \approx 0.5$. For the BER in a Cl^- -free electrolyte, a similar effect was observed (Fig. S8); Tafel curves in the range of $1\text{ mM} \leq [Br^-] \leq 100\text{ mM}$ had quasi-linear regions, but the slope at the onset of these quasi-linear regions itself depended on the concentration. The most straightforward interpretation of these results is a coverage effect of Br^* ; at the onset of the reaction, θ_{Br} is perhaps significantly high, and the Tafel slope is already changing from 40 to 120 mV/dec. It is also possible that repulsive adsorbate interactions (which are ignored by the Langmuir approximation) play a role. Alternatively, the change in slope may be caused by the formation of higher oxidation states in the IrO_x , which starts occurring in the same region where the BER is kinetically controlled [52]. The catalytic capability of IrO_x towards the OER has been shown to sensitively depend on this transition [53–55], such that it may also affect intrinsic rates of the BER. In any case, the theoretical upper limit of 120 mV/dec is never observed, possibly because diffusion limitations set in before the required overpotential is reached. To further investigate the bromide oxidation mechanism, we used Conway-Novák and Ferro-de Battisti test plots (Fig. S10), which offer a method to distinguish between the V-T or V-H mechanisms, respectively. The basis of this method is to rearrange the j vs. E relationship predicted by those mechanisms (i.e. Eq. (9) and Eq. (4)), to give a straight line; redrawing the experimental data in the same way and comparing the linearity provides a qualitative indication to which mechanism the data adhere the best. We found that both Conway-Novák and Ferro-de Battisti plots of the BER data resulted in linearity, but significantly diverged in the high overpotential limit; current densities in this region increased faster than expected by either mechanism, but Ferro-de Battisti plots gave better linearity overall. Similar results emerged from test plots involving bromide oxida-

tion in presence of Cl^- . Like the unusual Tafel slopes, it is possible that transient redox changes in the IrO_x play a role.

When HCl is added, competitive adsorption of Cl^- will take place. The Langmuir V-H and V-K mechanisms predict that, approximately, all Tafel slopes shift horizontally to lower potentials when this happens (see the SI for full details). The change in Tafel slopes in Fig. 2B versus $[HCl]$ qualitatively agrees with this, but the effect is rather subtle. We also note that \mathcal{R}_{Cl^-} for bromide oxidation is always negative; its value is predicted to be $\mathcal{R}_{Cl^-} = -\theta_{Cl}$ by both the V-H and V-K pathways, where $0 \leq \theta_{Cl} \leq 1$, such that the experimental value of -0.1 can be accommodated. The BER on IrO_x and the effect of Cl^- on this reaction can thus be modeled quite well by the V-H pathway, although describing the competitively adsorbing Br^* and Cl^* adsorbates with the Langmuir isotherm is likely an oversimplification.

As we saw previously on a Pt electrocatalyst [32], simultaneous adsorption of Cl^- during bromine evolution may lead to the formation of interhalogen products. Here, this can be excluded primarily because Cl^- has only a suppressive effect on the activity. If chloride was involved in any reaction, one would intuitively expect an increase in the mass-transport limited current densities of bromide oxidation. Instead, \mathcal{R}_{Cl^-} is close to zero in this region, suggesting that up until roughly 1.40 V vs. NHE, the BER is the only reaction occurring in a mixed $Br^- + Cl^-$ electrolyte.

3.4. UV-Vis studies of halogen evolution

At potentials near the onset of the CER and OER, the measured currents become increasingly convoluted. Although the formation of interhalogen compounds, like $BrCl$, could be excluded up to 1.40 V vs. NHE by kinetic analysis, it becomes difficult to unambiguously assign the disk activity to specific reactions at higher potentials. To reduce this complexity, we investigated the product distribution of halogen species near the surface using electrochemical UV-Vis spectroscopy. In these experiments, we increased the potential between 1.100 and 1.500 V vs. RHE in 25 mV steps, where

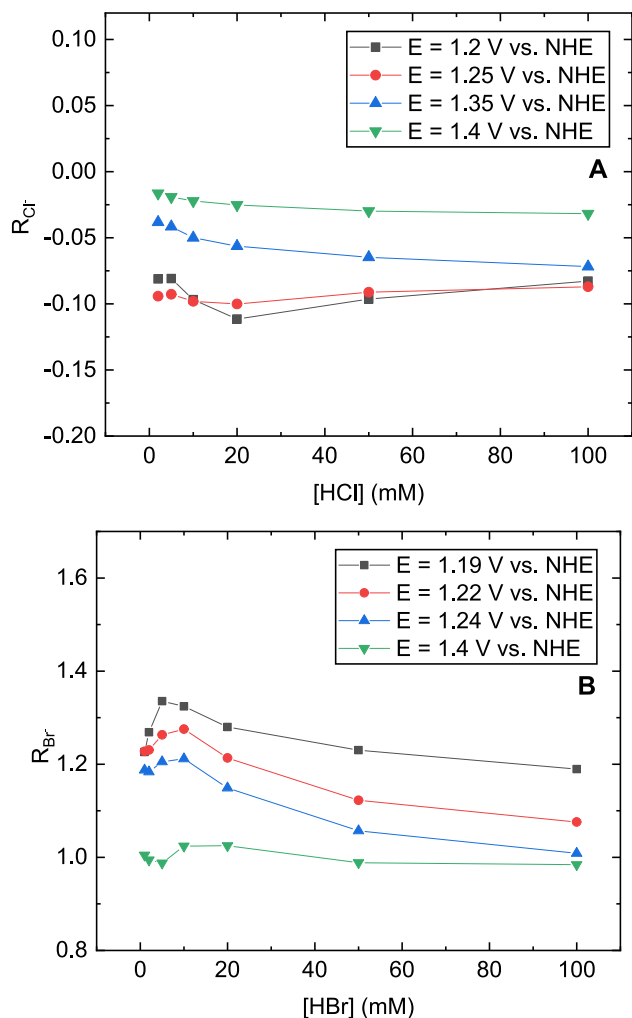
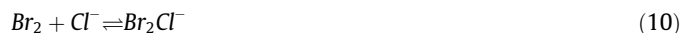


Fig. 3. Chloride reaction orders measured in the potential region of bromide oxidation, in 0.5 M $HClO_4$. Data are shown on the NHE potential scale to account for minor (± 4 mV) pH shifts. A: Chloride reaction orders R_{Cl^-} at several potentials, obtained by varying the HCl concentration at a fixed value $[HBr] = 10$ mM. B: Bromide reaction orders R_{Br^-} at several potentials, obtained by varying the HBr concentration in Cl^- -free conditions.

each step had a 30 s duration (Fig. S17). This way, the effect of increasing potential could be studied, as well as shifts in solution composition during progressive oxidation reactions for a given constant potential. Changes in the total transmission were measured after passing the beam through the back of the IrO_x/FTO electrodes and through the electrolyte. These experiments were carried out in 0.1 M $HClO_4 + 0.1$ M HCl, so that pH changes from HBr addition were negligible (on the order of 0.05 unit).

Of particular interest would be to study whether any kind of interhalogen formation occurs in the potential range in-between the BER and the CER. It must be noted that during electrolysis of a mixture of Br^- and Cl^- , interhalogen species are also formed chemically, through rapid follow-up reactions in solution such as:



Reactions as in Eq. (10) are a significant factor during UV-Vis experiments, where stationary electrodes are used. Interconversion of several interhalogen species are all extremely rapid reactions, so that any thermodynamically labile species will equilibrate over time. This unfortunately precludes the precise determination of species formed on the electrode surface, and also implies that measured UV-Vis data will always be the result of a

mixture of species. Fortunately, although we cannot pinpoint exactly the 'origin' (electrocatalytic or solution chemistry) of any halogen species near the electrode, we can still rationalize the occurrence of reactions happening in-between the BER and the CER from thermodynamic constraints. In case that only Br_2 is being generated at the electrode, large differences in equilibrium constants between species implies that no interhalogen other than Br_2Cl^- should be formed spontaneously in solution [32]. The occurrence of either $BrCl$ or $BrCl_2^-$ at electrode potentials lower than the thermodynamic onset of Cl_2 evolution can then only be rationalized by the occurrence of an electrochemical reaction.

It must be noted that the IrO_x catalyst layer itself is also UV-Vis active within the broad region 300–900 nm; potential-dependent differences in transmission due to the IrO_x layer were clearly visible in spectra taken in 0.1 M $HClO_4$ (see Fig. S20), and agree well with previously published results, including a notable red-shift at higher potentials of a species with a transmission minimum near 450 nm [54,56]. In order to observe only the contributions from solution (inter)halogen species, aforementioned difference spectra were subtracted from the difference spectra measured in presence of HBr and/or HCl.

Fig. 4 shows currents and the complete time-evolution of a typical UV-Vis experiment on an IrO_x/FTO electrode during the parallel oxidation of Br^- and Cl^- . The currents in Fig. 4A show the BER onset around 1.20 V vs. RHE, reaching a (diffusion-limited) peak at 1.325 V followed by the onset of a second reaction around 1.425 V vs. RHE. The latter is clearly due to the CER, and appears to be shifted to a ~ 50 mV higher potential compared to the CER in absence of Br^- , as was also observed in the RRDE experiments. The suppressive effect of Br^- on the chloride oxidation activity is also apparent. As shown in the corresponding UV-Vis spectra in Fig. 4B, all relevant (inter)halogen species have a secondary adsorption band (or shoulder, in case of Br_3^-) that falls in the range 325–400 nm. Up until 1.275 V vs. RHE, we observe mild adsorption with a broad shoulder spanning 340–450 nm, which suggests that the main species formed is Br_3^- [35]. Higher potentials then lead to the sustained growth of a peak around 385 nm, which can be attributed to the formation of Br_2 and Br_2Cl^- . The currents in Fig. 4A suggest that bromide oxidation starts to become transport limited around 1.30 V vs. RHE, depleting Br^- near the surface and reversing Br_3^- to Br_2 and Br_2Cl^- under the effect of Cl^- . This trend then persists over a rather wide potential range; up until 1.425 V vs. RHE, the only significant change is the growing of the Br_2 and Br_2Cl^- signals. Cl_2 starts to evolve around 1.450 V vs. RHE, coupled to a sharp decrease in transmission in the wavelengths corresponding to Cl_2 , $BrCl$ and $BrCl_2^-$. As Cl_2 is the most powerful oxidizer in the system under study, any interhalogen species previously described can now be formed in solution from follow-up reactions with Br^- . Crucially, we note that up until 1.425 V vs. RHE, the transmission within 335–345 nm is virtually constant, and we do not observe a shift of the peak around 385 nm to shorter wavelengths. Both observations suggest that $BrCl$ is not formed before the onset of the CER, which was a general finding during experiments with varying concentrations and ratios of $[Br^-]$ and $[Cl^-]$ (see also Fig. S19 and Fig. S21). Although we cannot exclude the formation of $BrCl$ in parallel with the CER, it seems reasonable that evolution of Cl_2 is the fastest and most prevalent reaction at the high potential limit. In the remainder of this paper, we will thus assume that the only major electrode reactions are the BER, CER and OER.

3.5. Kinetic analysis of chlorine and oxygen evolution

To investigate the CER and OER in the high potential region of Fig. 1A, the two reactions have to be separated from each other

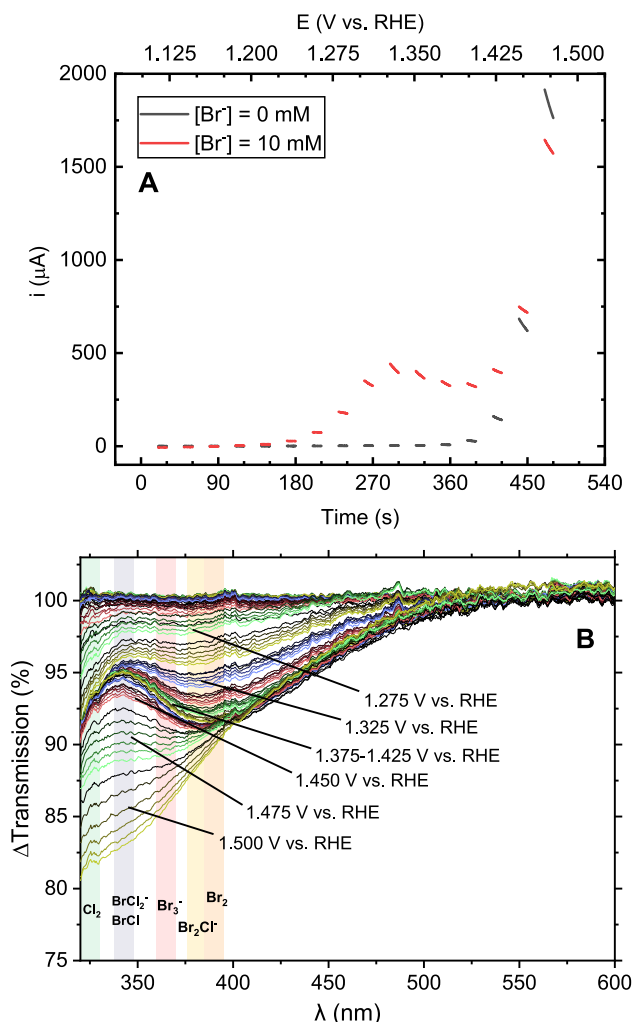


Fig. 4. UV-Vis measurements of a stationary IrO_x/FTO electrode in a solution of 0.1 M HClO₄ + 0.1 M HCl + 10 mM HBr. A: Currents measured during the experiment, where only the final 10 s of each potential step are shown for clarity (see Fig. S18 for full data). Currents in Br⁻-free conditions are shown for comparison, upper axis shows the potentials applied at each moment in time. B: Corresponding differences in transmission data of the region where the halogen species adsorb. Varying colors among traces correspond to different potential steps, of which some are indicated; color gradients from dark to light indicate time evolution of the spectra during each potential step. All spectra are difference spectra relative to 1.100 V vs. RHE, the contribution from the IrO_x layer was subtracted (see main text).

and the underlying BER. We will first describe a method for isolating and modeling these individual currents. As mentioned previously, the ring potential was optimized to selectively reduce halogen evolution products while leaving O₂ unreacted. When this condition is satisfied, the ring response is then proportional to j_{XER} , the total halogen evolution current density on the disk, according to

$$j_{XER} = |j_R/N| \quad (11)$$

where j_R is the ring current normalized to the disk geometrical surface area (therefore with the same units as j_D , mAcm⁻²_{disk}) and N is the ring-disk collection factor. From the ring currents, it is thus possible to derive j_{XER} , which is the sum of the BER and CER current densities, $j_{BER} + j_{CER}$ (Fig. S3A). Under the reasonable assumption that the IrO_x catalyst is stable, we may then assume that the remainder of j_D after subtraction of j_{XER} is due to OER:

$$j_{OER} = j_D - j_{XER} \quad (12)$$

After calculating j_{XER} from j_R , the CER must then be separated from the BER. A strict separation is complex, because the CER and BER are always superimposed, and the underlying contributions of each are not exactly known. However, the bromide oxidation wave generally is fully diffusion controlled at potentials higher than 1.40 V vs. NHE (see Section 3.1), implying that it follows a sigmoidal trend in the region that is obscured by the onset of chloride oxidation. We thus modeled the foot and the top of the bromide oxidation wave as sigmoidal curves using a 5-parameter generalised logistic function, similar to our previous work [32]. Due to competitive adsorption by Cl⁻ (Section 3.1), the wave can show notable asymmetry between the foot and the top. This asymmetry was nonetheless captured well by the relatively complex fitting functions (Fig. S3B). The generalised logistic function at the top of the wave was then used to extrapolate limiting current densities from bromide oxidation near the upper potential limit in j_{XER} . The remaining current density after subtraction can be assigned to the CER. Fig. S3 and Fig. S4 show an example of this procedure.

Fig. 5 shows the fitted and calculated individual current densities for the BER, CER and OER according to the above procedure. As previously established, the BER is suppressed by Cl⁻, illustrated by negative values for \mathcal{R}_{Cl^-} . The CER is mutually strongly inhibited by Br⁻, which shifts the onset potential for CER around 50 mV more positive (Fig. 5B). The OER is also negatively affected by Br⁻ (thick, green traces in Fig. 5C), and Cl⁻ further decreases the activity, showing that Br⁻ and Cl⁻ suppress the OER in an additive way. During measurements in 10 mM HBr and 100 mM HCl, the OER activity can become almost immeasurably small (Fig. 5C). At the same time, we observed that all measurable OER Tafel slopes are roughly similar, implying that the mechanism for oxygen evolution does not change under the effect of either Br⁻ and Cl⁻ (Fig. S14B). The retardation of the reaction is then probably caused by active site blocking.

From the partial current densities in Fig. 5, it is possible to determine Tafel slopes for the CER, as well as values of \mathcal{R}_{Cl^-} in presence and absence of Br⁻, as shown in Figs. 6 and 7.

In Fig. 6B, Tafel slopes for the CER competing with the OER generally start close to 40 mV/dec and then steadily increase. It is interesting to note that measurements in low [HCl] (such as 2 mM) show a sharp rise of the slope above 120 mV/dec, like the BER in Section 3.3. The reason is probably the onset of diffusion limitations, as the rates measured at the high potential limit were within 40–50% of the Levich limiting current density for the 2–5 mM experiments. At chloride concentrations higher than 5 mM, the Levich limiting current density was approached less closely; diffusion control thus becomes less of a factor, implying that the reaction kinetics are slowed down as a result of the increasing [Cl⁻].

When comparing Fig. 6B to data in Fig. 6A, the upward curvature in the high potential limits disappears in the presence of Br⁻, as can be explained by the much lower overall reaction rates and thus the virtual absence of diffusion control (see Fig. 5B). Linear Tafel slopes in Fig. 6A start around 30 mV/dec, within 1.49–150 V vs. NHE, which is slightly lower than 40 mV/dec. These values seemingly agree with predictions by the Volmer-Tafel mechanism, but are more likely related to errors in the model describing the underlying BER limiting current density, which possibly approaches the real limiting value too quickly. These errors had low absolute values, but are magnified in the region where the CER current density is also still small.

Fig. 7 shows \mathcal{R}_{Cl^-} values for the CER and the effect of Br⁻ (see Fig. S15). Br⁻ strongly lowers the activity of the CER, and at the same time, reaction orders are higher when comparing Fig. 7A and B, where in the latter, values are usually below 1. All values decrease with increasing [Cl⁻]. Higher reaction orders can be

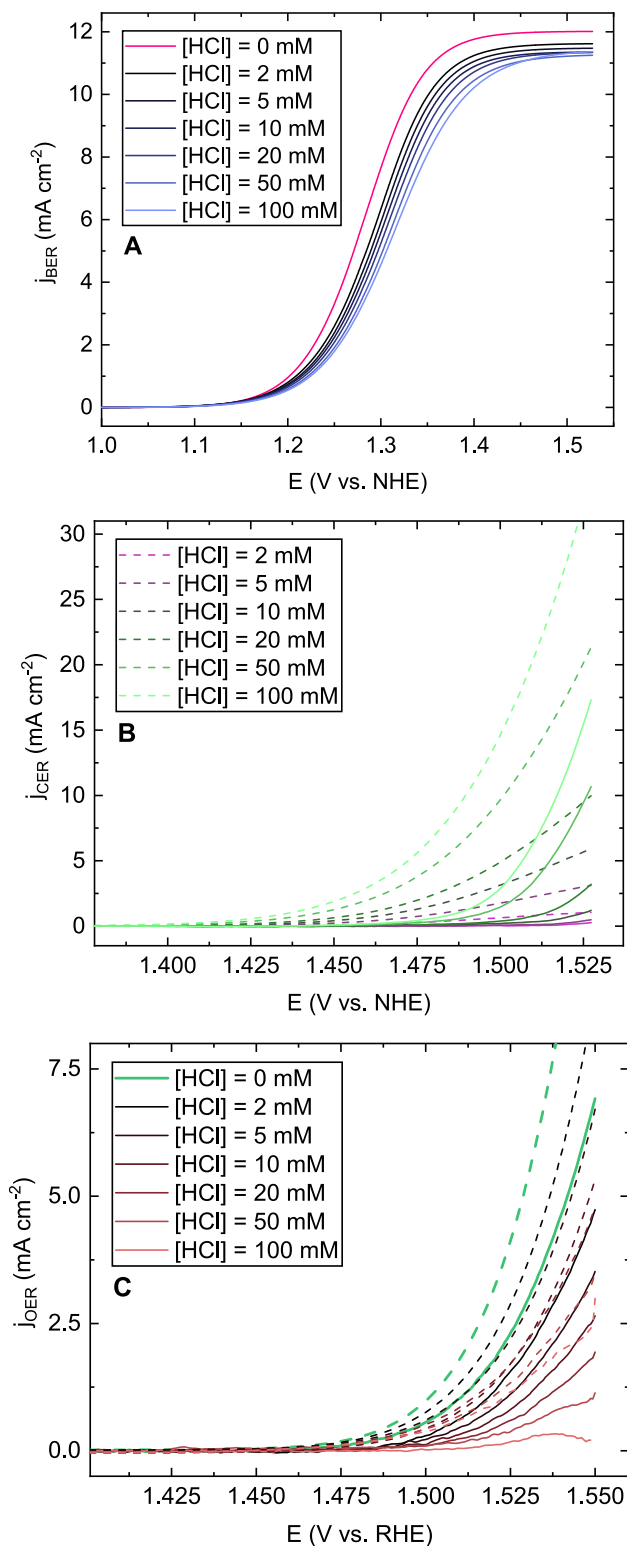


Fig. 5. Individual BER, CER and OER current densities during parallel Br^- , Cl^- and H_2O oxidation as function of $[HCl]$, on an IrO_x/GC electrode in 0.5 M $HClO_4$ and 10 mM HBr. A: BER current densities derived from generalized logistic fits of the foot and top of BER waves in Fig. 1A. Pink trace shows chloride-free conditions. B and C: CER and OER current densities derived from BER logistic fits and the ring response. Solid traces show CER (B) and OER (C) in presence of 10 mM HBr. Dashed traces are similar experiments in solutions free of Br^- . Green, solid trace in C shows OER measured in 0.5 M $HClO_4$ and 10 mM HBr only (no Cl^-). Green, dashed trace in C shows ‘pure OER’, measured in 0.5 M $HClO_4$ (no Cl^- and Br^-).

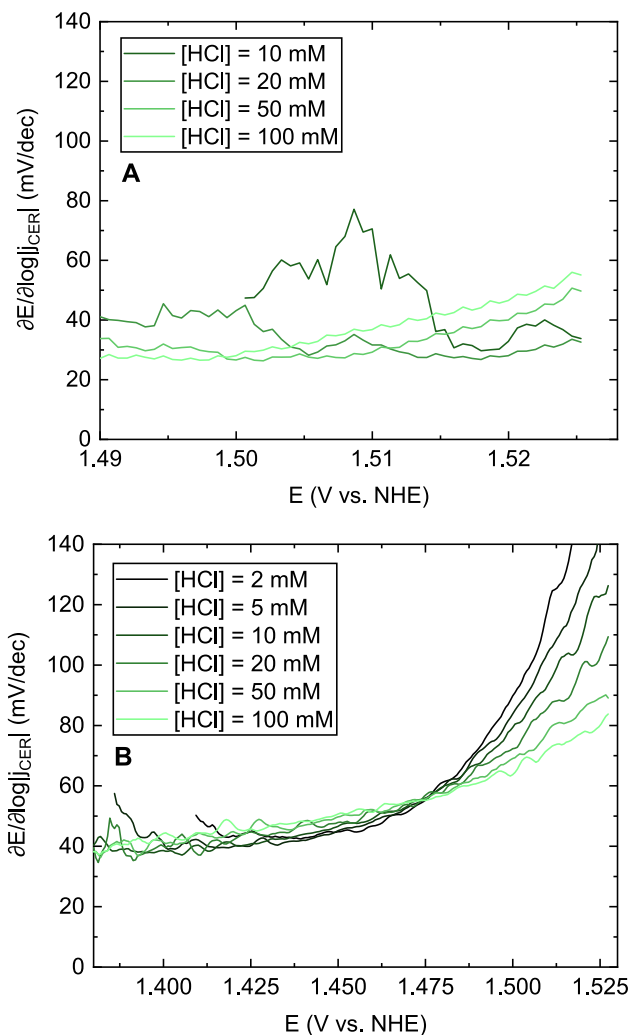


Fig. 6. CER Tafel slopes, measured in presence (A) and absence (B) of 10 mM HBr, based on data from Fig. 5. Data for chloride concentrations lower than 10 mM in A had insufficient signal to noise ratio and were omitted.

expected when competitive adsorption by Br^- decreases the chloride surface coverage θ_{Cl} . A lower value of θ_{Cl} at the onset of the reaction means its contribution to the measured reaction order is higher (see Section 3.2 and the SI). The range of values spanned by \mathcal{R}_{Cl^-} in Fig. 7A is mostly within 1–2, agreeing with the V-H mechanism; only the value at the highest $[Cl^-]$ is around 0.8, which falls outside of this range. Corresponding Tafel data for $[Cl^-] = 50$ mM and 100 mM in Fig. 6A, which are the most accurate, are lower than in Fig. 6B, but display roughly the same rate of change over the measured potential window. This suggests that like the BER, the Tafel slopes as a whole are shifted on the potential axis. Together with the rising Tafel slopes as function of potential, this may be a coverage effect by Cl^* when considering V-H or V-K as the dominant mechanism. We further analyzed the CER using Conway-Novak and Ferro-de Battisti test plots, which clearly point towards a V-H or V-K type mechanism for the CER, including when the reaction is inhibited by Br^- (Fig. S13). It must be noted that linearity in Ferro-de Battisti test plots does not discern between the V-H and V-K mechanism, as their functional j vs. E relationship is the same. Distinction is in principle possible by investigating values of the slopes and y -intercepts, but we refrained from this

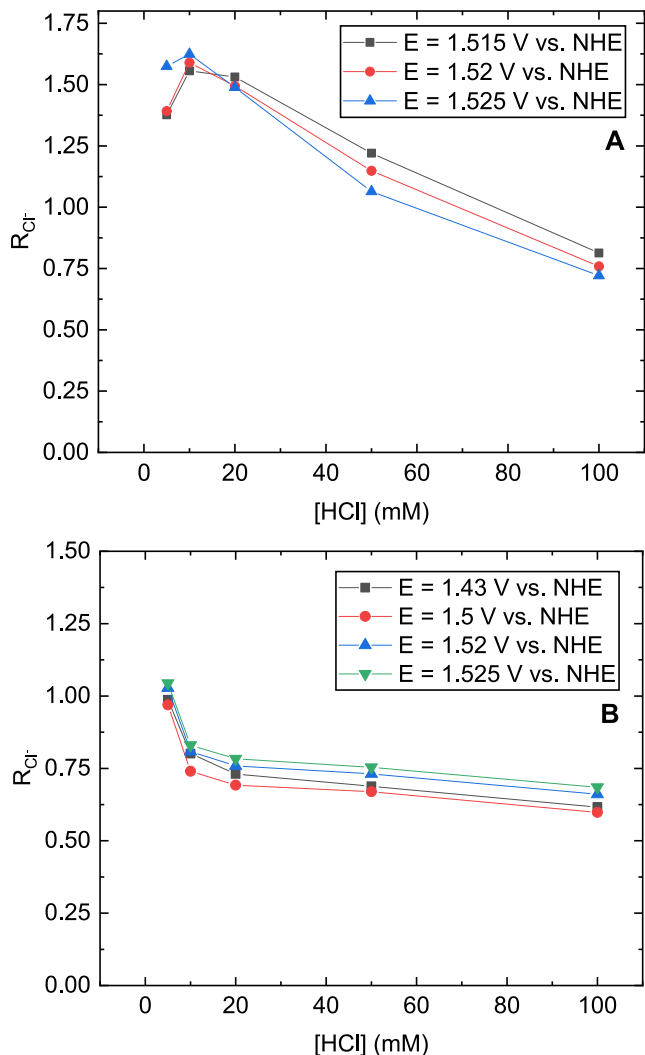


Fig. 7. Chloride reaction orders \mathcal{R}_{Cl^-} for the CER, in presence (A) and absence (B) of 10 mM HBr, based on data from Fig. 5. Potentials were chosen to span the range where significant CER occurs, which is much narrower for the CER in presence of Br^- . Data in B are only shown for $[Cl^-]$ values where the ring collection method is reliable [36].

because these quantities are extremely sensitive to the value of the equilibrium potential, and become further convoluted when competitive adsorption is involved. It is in any case most likely that the values for \mathcal{R}_{Cl^-} in Fig. 7A and B correspond to V-H or V-K mechanisms with a first-order dependence on θ_{Cl^-} .

Finally, we note that the significant depressing effect of Cl^- on the OER activity is in stark contrast with our previous study [36], where the same IrO_x/GC electrode was studied for the CER. In a 0.5 M $KHSO_4$ electrolyte, Cl^- has only a negligible effect on the OER activity, and the reaction order for the CER approaches values slightly <1 (see Fig. S15). It is likely the presence of HSO_4^- that negates the suppressive effect of Cl^- on the OER and CER, because OER and CER activities in such electrolytes were significantly lower than in a solution of non-adsorbing ClO_4^- . This strengthens the idea that chloride effects on CER and OER in the current study are related to specific adsorption of Cl^- . In presence of excess HSO_4^- , the surface is already heavily under the influence of a competitive adsorbate. Addition of Cl^- would then have a much smaller effect on the activity, because the reaction order effect from competitive adsorption is already near saturation. These results illustrate that specific adsorption by the supporting electrolyte can have a signif-

icant effect on the apparent kinetics of the reaction, and should be kept in mind when investigating concentration-dependent quantities.

3.6. Molar selectivities

We finally consider the selectivities of the BER, CER and OER as function of the various halogen anion concentrations, which can be derived from data in Fig. 5. Molar selectivities ε of the BER, CER and OER can be calculated for a given value of E or $[Cl^-]$ via

$$\varepsilon_{BER} = \frac{j_{BER}/2}{j_{BER}/2 + j_{CER}/2 + j_{OER}/4} \quad (13)$$

In Eq. (13), the BER molar selectivity is given as example; each reaction is corrected for the number of electrons. Fig. 8 shows some measured selectivities of the three reactions.

At lower potentials, the BER has near 100% selectivity, since it is the only possible reaction up until ~ 1.37 V. The CER has a significant overpotential due to the suppressive effect of Br^- , and onsets at around the same potential as the OER; the BER is virtually 100%

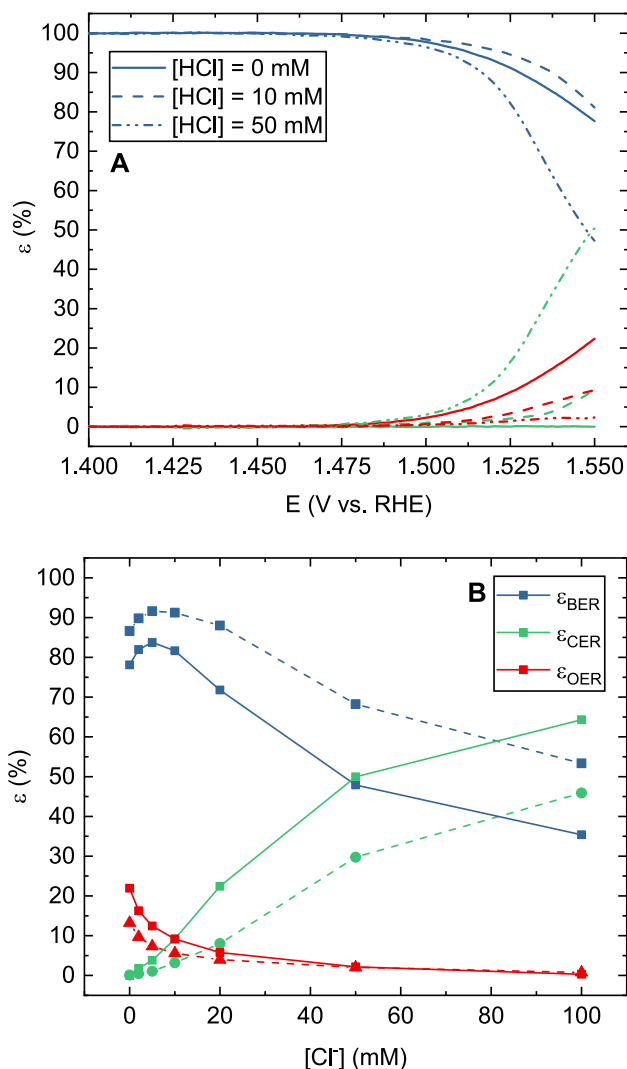


Fig. 8. Molar selectivities of the BER, CER, and OER in 0.5 M $HClO_4$ + 10 mM HBr. A: Data as function of potential, at chloride concentrations of 0 (solid trace), 10 (dashed trace) and 50 mM (dotted trace). Blue, green and red show selectivities for BER, CER and OER, respectively. B: Data as function of chloride concentration at potentials of 1.535 (dashed trace) and 1.55 V vs. RHE (solid trace). These are potentials where all three reactions are prevalent.

mass transport controlled at this point. Addition of Cl^- has a two-fold effect on ϵ_{BER} , as it is decreased by the onset of the CER, but also increased due to suppression of the OER by Cl^- . This effect is especially visible in Fig. 8B where Cl^- increases the BER selectivity up until 10 mM Cl^- , after which it decreases again with increasing CER competition. Another peculiarity of kinetic interplay arises when inspecting the OER and CER selectivities relative to each other, and the effect of bromide. From Fig. S16, when the CER and OER are the only reactions, the OER selectivity always increases with higher potential. In presence of Br^- however, the selectivity decreases.

OER selectivity is always quite low (<22%), and sharply decreases when Cl^- is added; <1% O_2 is formed at 100 mM Cl^- . On the other hand, the OER is much less sensitive to mass transport effects in an aqueous electrolyte, and should therefore still become the dominant reaction as the potential is further increased above 1.55 V vs. RHE. However, the overpotential where this happens will be dependent on Br^- and Cl^- in dual fashion; besides the parallel BER and CER contributions, which must be outpaced, Br^- and Cl^- additionally impart significant kinetic suppression on OER itself and make the reaction even more sluggish. We were unfortunately not able to measure reliable data at potentials higher than 1.55 V vs. RHE, because the increasing OER rates lead to persistent O_2 bubbles on the RRDE tip which compromise the measurements [41]. We expect that generally, the selectivity trends of OER versus halogen oxidation such as in this study will depend sensitively on the electrode material, mass transport conditions and electrolyte composition. They illustrate that intricate interplay between kinetics can already have significant consequences at small reactant concentrations. The possible effects of Br^- in the context of saline water electrolysis, even when present in small amounts, must thus not be underestimated.

4. Conclusions

In this work, we studied the simultaneous oxidation of Br^- , Cl^- and H_2O on GC-supported IrO_x , which served to emulate an OER catalyst in acidic electrolyzers. Adsorption and oxidation of Br^- and Cl^- proceeded simultaneously and had notable mutual effects on their respective evolution reactions. Bromine evolution exhibited reaction orders $\mathcal{R}_{\text{Br}^-}$ that are significantly higher than 1 at kinetically controlled potentials, but semi-linear Tafel slopes of 90–110 mV/dec; chloride addition shifted the slopes to slightly higher values and was associated with mildly inhibiting effects ($\mathcal{R}_{\text{Cl}^-} \approx -0.1$). Together with the use of test plots, the Volmer-Heyrovský mechanism with a Langmuirian isotherm describing competitive adsorption of the halogen anions seems to describe the BER mechanism on IrO_x the most adequately. The CER displays previously reported linear Tafel slopes of ~ 40 mV/dec, also in presence of Br^- ; chloride reaction orders had values $0.7 < \mathcal{R}_{\text{Cl}^-} < 1$, but under the effect of Br^- they were significantly higher than 1. Together with test plots, the Volmer-Heyrovský again is the most suitable description for the experimental results.

The OER was particularly slowed down by a compounded effect of both Br^- and Cl^- ; like the effects observed for the CER, the nature of this effect seemed to be a type of ‘simple’ competitive adsorption through site blocking, as the Tafel slopes (and therefore the underlying mechanism) did not change significantly. The selectivity for the OER was close to 0 at 1.55 V vs. RHE in conditions of 10 mM HBr and 100 mM HCl, which were the maximum concentrations tested. Contrary to findings on Pt in a previous paper, no signs of BrCl formation were observed, even though Br^- and Cl^- interact strongly during adsorption. Kinetic analysis of the bromide oxidation region and UV–Vis experiments suggested that the only electrochemically formed products are Br_2 , Cl_2 and O_2 .

Acknowledgments

This research received funding from the Netherlands Organization for Scientific Research (NWO) in the framework of the fund New Chemical Innovations, project 731.015.204 ELECTROGAS, with financial support of Akzo Nobel Chemicals, Shell Global Solutions, Magneto Special Anodes (an Evoqua Brand) and Elson Technologies.

References

- [1] T.R. Cook, D.K. Dogutan, S.Y. Reece, Y. Surendranath, T.S. Teets, D.G. Nocera, Solar energy supply and storage for the legacy and nonlegacy worlds, *Chem. Rev.* 110 (11) (2010) 6474–6502, <https://doi.org/10.1021/cr100246c>.
- [2] I. Staffell, D. Scamman, A. Velazquez Abad, P. Balcombe, P.E. Dodds, P. Ekins, N. Shah, K.R. Ward, The role of hydrogen and fuel cells in the global energy system, *Energy Environ. Sci.* 12 (2) (2019) 463–491, <https://doi.org/10.1039/C8EE01157E>.
- [3] O. Schmidt, A. Gambhir, I. Staffell, A. Hawkes, J. Nelson, S. Few, Future cost and performance of water electrolysis: an expert elicitation study, *Int. J. Hydrogen Energy* 42 (52) (2017) 30470–30492, <https://doi.org/10.1016/j.ijhydene.2017.10.045>.
- [4] J.E. Bennett, Electrodes for generation of hydrogen and oxygen from seawater, *Int. J. Hydrogen Energy* 5 (4) (1980) 401–408, [https://doi.org/10.1016/0360-3199\(80\)90021-X](https://doi.org/10.1016/0360-3199(80)90021-X).
- [5] S. Dresp, F. Dionigi, M. Klingenhof, P. Strasser, Direct electrolytic splitting of seawater: opportunities and challenges, *ACS Energy Lett.* 4 (4) (2019) 933–942, <https://doi.org/10.1021/acsenergylett.9b00220>.
- [6] J. Juodkazytė, B. Šebeka, I. Savickaja, M. Petrulėvičienė, S. Butkutė, V. Jasulaitienė, A. Selskis, R. Ramanauskas, Electrolytic splitting of saline water: durable nickel oxide anode for selective oxygen evolution, *Int. J. Hydrogen Energy* 44 (12) (2019) 5929–5939, <https://doi.org/10.1016/j.ijhydene.2019.01.120>.
- [7] Y. Jung, E. Hong, Y. Yoon, M. Kwon, J. Kang, Formation of bromate and chlorate during ozonation and electrolysis in seawater for ballast water treatment, *Ozone Sci. Eng.* 36 (6) (2014) 515–525, <https://doi.org/10.1080/01919512.2014.956862>.
- [8] A. El-Moneim, N. Kumagai, K. Asami, K. Hashimoto, Nanocrystalline manganese-molybdenum-tungsten oxide anodes for oxygen evolution in acidic seawater electrolysis, *Mater. Trans.* 46 (2) (2005) 309–316, <https://doi.org/10.2320/matertrans.46.309>.
- [9] F. Dionigi, T. Reier, Z. Pawolek, M. Gliech, P. Strasser, Design criteria, operating conditions, and nickel-iron hydroxide catalyst materials for selective seawater electrolysis, *ChemSusChem* 9 (9) (2016) 962–972, <https://doi.org/10.1002/cssc.201501581>.
- [10] S. Trasatti, Electrocatalysis in the anodic evolution of oxygen and chlorine, *Electrochim. Acta* 29 (11) (1984) 1503–1512, [https://doi.org/10.1016/0013-4686\(84\)85004-5](https://doi.org/10.1016/0013-4686(84)85004-5).
- [11] J.E. Yourey, K.J. Pyper, J.B. Kurtz, B.M. Bartlett, Chemical stability of CuWO_4 for photoelectrochemical water oxidation, *J. Phys. Chem. C* 117 (17) (2013) 8708–8718, <https://doi.org/10.1021/jp402048b>.
- [12] V. Petrykin, K.M. Macounová, O. Shlyakhtin, P. Krtil, Tailoring the selectivity for electrocatalytic oxygen evolution on ruthenium oxides by zinc substitution, *Angew. Chemie Int. Ed.* 49 (28) (2010) 4813–4815, <https://doi.org/10.1002/anie.200907128>.
- [13] B.E. Conway, D.M. Novák, Chloride ion adsorption effects in the recombination-controlled kinetics of anodic chlorine evolution at Pt electrodes, *J. Chem. Soc. Faraday Trans. Phys. Chem. Condens. Phases* 75 (1979) 2454–2472, <https://doi.org/10.1039/F19797502454>.
- [14] B.E. Conway, Y. Phillips, S. Qian, Surface electrochemistry and kinetics of anodic bromine formation at platinum, *J. Chem. Soc., Faraday Trans.* 91 (2) (1995) 283, <https://doi.org/10.1039/ft9959100283>.
- [15] I.C. Man, *Theoretical Study of Electro-Catalysts for Oxygen Evolution*, Technical University of Denmark, 2011.
- [16] J.A. Harrison, S.D. Hermijanto, The oxidation of chloride ions and bromide ions on ruthenium dioxide electrodes, *J. Electroanal. Chem. Interfacial Electrochem.* 225 (1–2) (1987) 159–175, [https://doi.org/10.1016/0022-0728\(87\)80011-6](https://doi.org/10.1016/0022-0728(87)80011-6).
- [17] M.T.M. Koper, Thermodynamic theory of multi-electron transfer reactions: implications for electrocatalysis, *J. Electroanal. Chem.* 660 (2) (2011) 254–260, <https://doi.org/10.1016/j.jelechem.2010.10.004>.
- [18] H. Dau, C. Limberg, T. Reier, M. Risch, S. Roggan, P. Strasser, The mechanism of water oxidation: from electrolysis via homogeneous to biological catalysis, *ChemCatChem* 2 (7) (2010) 724–761, <https://doi.org/10.1002/cctc.201000126>.
- [19] N. Suen, S. Hung, Q. Quan, N. Zhang, Y. Xu, H. Chen, Electrocatalysis for the oxygen evolution reaction: recent development and future perspectives, *Chem. Soc. Rev.* 46 (2) (2017) 337–365, <https://doi.org/10.1039/C6CS00328A>.
- [20] M. Tahir, L. Pan, F. Idrees, X. Zhang, L. Wang, J. Zou, Z.L. Wang, Electrocatalytic oxygen evolution reaction for energy conversion and storage: a comprehensive review, *Nano Energy* 37 (May) (2017) 136–157, <https://doi.org/10.1016/j.nanoen.2017.05.022>.
- [21] R.K.B. Karlsson, A. Cornell, Selectivity between oxygen and chlorine evolution in the Chlor-Alkali and chlorate processes, *Chem. Rev.* 116 (5) (2016) 2982–3028, <https://doi.org/10.1021/acs.chemrev.5b00389>.

- [22] I. Moussallem, J. Jörissen, U. Kunz, S. Pinnow, T. Turek, Chlor-Alkali electrolysis with oxygen depolarized cathodes: history, present status and future prospects, *J. Appl. Electrochem.* 38 (9) (2008) 1177–1194, <https://doi.org/10.1007/s10800-008-9556-9>.
- [23] K. Saadi, P. Nanikashvili, Z. Tatus-Portnoy, S. Hardisty, V. Shokhen, M. Zysler, D. Zitoun, Crossover-tolerant coated platinum catalysts in hydrogen/bromine redox flow battery, *J. Power Sources* 422 (6) (2019) 84–91, <https://doi.org/10.1016/j.jpowsour.2019.03.043>.
- [24] N. Venkatesan, K.S. Archana, S. Suresh, R. Aswathy, M. Ulaganthan, P. Periasamy, P. Ragupathy, Boron-doped graphene as efficient electrocatalyst for zinc-bromine redox flow batteries, *ChemElectroChem* 6 (4) (2019) 1107–1114, <https://doi.org/10.1002/celec.201801465>.
- [25] S. Schulz, H.H. Hahn, Generation of halogenated organic compounds in municipal waste water, in: *Water Science and Technology*, 1998, [https://doi.org/10.1016/S0273-1223\(97\)00782-8](https://doi.org/10.1016/S0273-1223(97)00782-8).
- [26] Y. Sun, Q. Wu, H. Hu, J. Tian, Effect of bromide on the formation of disinfection by-products during wastewater chlorination, *Water Res.* 43 (9) (2009) 2391–2398, <https://doi.org/10.1016/j.watres.2009.02.033>.
- [27] C. Tian, R. Liu, T. Guo, H. Liu, Q. Luo, J. Qu, Chlorination and chloramination of high-bromide natural water: DBPs species transformation, *Sep. Purif. Technol.* 102 (2013) 86–93, <https://doi.org/10.1016/j.seppur.2012.09.034>.
- [28] H. Yalçın, T. Koç, V. Pamuk, Hydrogen and bromine production from concentrated sea-water, *Int. J. Hydrogen Energy* 22 (10–11) (1997) 967–970, [https://doi.org/10.1016/S0360-3199\(96\)00214-5](https://doi.org/10.1016/S0360-3199(96)00214-5).
- [29] I. Cohen, B. Shapira, E. Avraham, A. Soffer, D. Aurbach, Bromide ions specific removal and recovery by electrochemical desalination, *Environ. Sci. Technol.* 52 (11) (2018) 6275–6281, <https://doi.org/10.1021/acs.est.8b00282>.
- [30] M.B. Heeb, J. Criquet, S.G. Zimmermann-Steffens, U. von Gunten, Oxidative treatment of bromide-containing waters: formation of bromine and its reactions with inorganic and organic compounds – a critical review, *Water Res.* 48 (1) (2014) 15–42, <https://doi.org/10.1016/j.watres.2013.08.030>.
- [31] R.S. Magazinovic, B.C. Nicholson, D.E. Mulcahy, D.E. Davey, Bromide levels in natural waters: its relationship to levels of both chloride and total dissolved solids and the implications for water treatment, *Chemosphere* 57 (4) (2004) 329–335, <https://doi.org/10.1016/j.chemosphere.2004.04.056>.
- [32] J.G. Vos, A. Venugopal, W.A. Smith, M.T.M. Koper, Competition and interhalogen formation during parallel electrocatalytic oxidation of bromide and chloride on Pt, *J. Electrochem. Soc.* 167 (4) (2020) 046505, <https://doi.org/10.1149/1945-7111/ab717c>.
- [33] Q. Liu, D.W. Margerum, Equilibrium and kinetics of bromine chloride hydrolysis, *Environ. Sci. Technol.* 35 (6) (2001) 1127–1133, <https://doi.org/10.1021/es001380r>.
- [34] R.C. Beckwith, T. Wang, D.W. Margerum, Equilibrium and kinetics of bromine hydrolysis, *Inorg. Chem.* 35 (4) (1996) 995–1000, <https://doi.org/10.1021/ic950909w>.
- [35] T. Wang, M.D. Kelley, J.N. Cooper, R.C. Beckwith, D.W. Margerum, Equilibrium, kinetic, and UV-spectral characteristics of aqueous bromine chloride, bromine, and chlorine species, *Inorg. Chem.* 33 (25) (1994) 5872–5878, <https://doi.org/10.1021/ic00103a040>.
- [36] J.G. Vos, M.T.M. Koper, Measurement of competition between oxygen evolution and chlorine evolution using rotating ring-disk electrode voltammetry, *J. Electroanal. Chem.* (2017), <https://doi.org/10.1016/j.jelechem.2017.10.058>.
- [37] T. Nakagawa, C.A. Beasley, R.W. Murray, Efficient electro-oxidation of water near its reversible potential by a mesoporous IrO_x nanoparticle film, *J. Phys. Chem. C* 113 (30) (2009) 12958–12961, <https://doi.org/10.1021/jp9060076>.
- [38] Y. Zhao, N.M. Vargas-Barbosa, E.A. Hernandez-Pagan, T.E. Mallouk, Anodic deposition of colloidal iridium oxide thin films from hexahydroxyiridate(IV) solutions, *Small* 7 (14) (2011) 2087–2093, <https://doi.org/10.1002/sml.201100485>.
- [39] Y. Zhao, E.A. Hernandez-Pagan, N.M. Vargas-Barbosa, J.L. Dysart, T.E. Mallouk, A high yield synthesis of ligand-free iridium oxide nanoparticles with high electrocatalytic activity, *J. Phys. Chem. Lett.* 2 (5) (2011) 402–406, <https://doi.org/10.1021/jz200051c>.
- [40] J.G. Vos, T. Wezendonk, A.W. Jeremiasse, M.T.M. Koper, MnOx/IrOx as selective oxygen evolution electrocatalyst in acidic chloride solution, *J. Am. Chem. Soc.* 140 (32) (2018) 10270–10281, <https://doi.org/10.1021/jacs.8b05382>.
- [41] J.G. Vos, M.T.M. Koper, Examination and prevention of ring collection failure during gas-evolving reactions on a rotating ring-disk electrode, *J. Electroanal. Chem.* 850 (2019) 113363, <https://doi.org/10.1016/j.jelechem.2019.113363>.
- [42] S. Vesztergom, N. Barankai, N. Kovács, M. Ujvári, T. Wandlowski, G.G. Láng, Rotating ring-disk electrode with dual dynamic potential control: theory and practice, *Acta Chim. Slov.* 61 (2) (2014) 223–232.
- [43] N.M. Marković, H.A. Gasteiger, B.N. Grgr, P.N. Ross, Oxygen reduction reaction on Pt(111): effects of bromide, *J. Electroanal. Chem.* 467 (1) (1999) 157–163, [https://doi.org/10.1016/S0022-0728\(99\)00020-0](https://doi.org/10.1016/S0022-0728(99)00020-0).
- [44] C.C.L. McCrory, S. Jung, J.C. Peters, T.F. Jaramillo, Benchmarking heterogeneous electrocatalysts for the oxygen evolution reaction, *J. Am. Chem. Soc.* 135 (45) (2013) 16977–16987, <https://doi.org/10.1021/ja407115p>.
- [45] L.I. Krishtalik, Kinetics and mechanism of anodic chlorine and oxygen evolution reactions on transition metal oxide electrodes, *Electrochim. Acta* 26 (3) (1981) 329–337, [https://doi.org/10.1016/0013-4686\(81\)85019-0](https://doi.org/10.1016/0013-4686(81)85019-0).
- [46] V. Consonni, S. Trasatti, F.H. Pollak, W.E. O'Grady, Mechanism of chlorine evolution on oxide anodes: study of PH effects, *J. Electroanal. Chem.* 228 (1–2) (1987) 393–406, [https://doi.org/10.1016/0022-0728\(87\)80119-5](https://doi.org/10.1016/0022-0728(87)80119-5).
- [47] S. Trasatti, Progress in the understanding of the mechanism of chlorine evolution at oxide electrodes, *Electrochim. Acta* 32 (3) (1987) 369–382, [https://doi.org/10.1016/0013-4686\(87\)85001-6](https://doi.org/10.1016/0013-4686(87)85001-6).
- [48] B.V. Tilak, B.E. Conway, Analytical relations between reaction order and tafel slope derivatives for electrocatalytic reactions involving chemisorbed intermediates, *Electrochim. Acta* 37 (1) (1992) 51–63, [https://doi.org/10.1016/0013-4686\(92\)80011-A](https://doi.org/10.1016/0013-4686(92)80011-A).
- [49] M.H.P. Santana, L.A. De Faria, Oxygen and chlorine evolution on RuO₂ + TiO₂ + CeO₂ + Nb₂O₅ mixed oxide electrodes, *Electrochim. Acta* 51 (17) (2006) 3578–3585, <https://doi.org/10.1016/j.electacta.2005.09.050>.
- [50] R. Boggio, A. Carugati, G. Lodi, S. Trasatti, Mechanistic study of Cl₂ evolution at Ti-supported Co₃O₄ anodes, *J. Appl. Electrochem.* 15 (3) (1985) 335–349, <https://doi.org/10.1007/BF00615986>.
- [51] D.A. Denton, J.A. Harrison, R.I. Knowles, Chlorine evolution and reduction on RuO₂/TiO₂ electrodes, *Electrochim. Acta* 24 (5) (1979) 521–527, [https://doi.org/10.1016/0013-4686\(79\)85027-6](https://doi.org/10.1016/0013-4686(79)85027-6).
- [52] P. Steegstra, M. Busch, I. Panas, E. Ahlberg, Revisiting the redox properties of hydrous iridium oxide films in the context of oxygen evolution, *J. Phys. Chem. C* 117 (40) (2013) 20975–20981, <https://doi.org/10.1021/jp407030r>.
- [53] A. Minguzzi, O. Lugaresi, E. Achilli, C. Locatelli, A. Vertova, P. Ghigna, S. Rondinini, Observing the oxidation state turnover in heterogeneous iridium-based water oxidation catalysts, *Chem. Sci.* 5 (9) (2014) 3591–3597, <https://doi.org/10.1039/C4SC00975D>.
- [54] H. Ooka, A. Yamaguchi, T. Takashima, K. Hashimoto, R. Nakamura, Efficiency of oxygen evolution on iridium oxide determined from the PH dependence of charge accumulation, *J. Phys. Chem. C* 121 (33) (2017) 17873–17881, <https://doi.org/10.1021/acs.jpcc.7b03749>.
- [55] A. Minguzzi, C. Locatelli, O. Lugaresi, E. Achilli, G. Cappelletti, M. Scavini, M. Coduri, P. Masala, B. Sacchi, A. Vertova, et al., Easy accommodation of different oxidation states in iridium oxide nanoparticles with different hydration degree as water oxidation electrocatalysts, *ACS Catal.* 5 (9) (2015) 5104–5115, <https://doi.org/10.1021/acscatal.5b01281>.
- [56] H. Ooka, Y. Wang, A. Yamaguchi, M. Hatakeyama, S. Nakamura, K. Hashimoto, R. Nakamura, Legitimate intermediates of oxygen evolution on iridium oxide revealed by in situ electrochemical evanescent wave spectroscopy, *PCCP* 18 (22) (2016) 15199–15204, <https://doi.org/10.1039/C6CP02385A>.